BIOCHEMISTRY
including biophysical chemistry & molecular biology

Article

pubs.acs.org/biochemistry

An Oligomeric C-RING Nacre Protein Influences Prenucleation Events and Organizes Mineral Nanoparticles

Iva Perovic,[†] Andreas Verch,[§] Eric P. Chang,[†] Ashit Rao,[‡] Helmut Cölfen,[‡] Roland Kröger,[§] and John Spencer Evans*[,†]

[†]Laboratory for Chemical Physics, Division of Basic Sciences, and Center for Skeletal Biology, New York University, 345 East 24th Street, New York, New York 10010, United States

[‡]Department of Chemistry, Physical Chemistry, Universität Konstanz, Universitätstrasse 10, D-78457 Konstanz, Germany

[§]Department of Physics, University of York, Heslington, York YO10 5DD, U.K.

Supporting Information

ABSTRACT: The mollusk shell nacre layer integrates mineral phases with macromolecular components such as intracrystalline proteins. However, the roles performed by intracrystalline proteins in calcium carbonate nucleation and subsequent postnucleation events (e.g., organization of mineral deposits) in the nacre layer are not known. We find that AP7, a nacre intracrystalline C-RING protein, self-assembles to form amorphous protein oligomers and films on mica that further assemble into larger aggregates or phases in the presence of Ca^{2+}. Using solution nuclear magnetic resonance spectroscopy, we determine that the protein assemblies are stabilized by interdomain interactions involving the aggregation-prone T31−N66 C-terminal C-RING domain but are destabilized by the labile nature of the intrinsically disordered D1−T19 AA N-terminal sequence. Thus, the dynamic, amorphous nature of the AP7 assemblies can be traced to the molecular behavior of the N-terminal sequence. Using potentiometric methods, we observe that AP7 protein phases prolong the time interval for prenucleation cluster formation but neither stabilize nor destabilize ACC clusters. Time-resolved flow cell scanning transmission electron microscopy mineralization studies confirm that AP7 protein phases delay the onset of nucleation and assemble and organize mineral nanoparticles into ring-shaped branching clusters in solution. These phenomena are not observed in protein-deficient assays. We conclude that C-RING AP7 protein phases modulate the time period for early events in nucleation and form strategic associations with forming mineral nanoparticles that lead to mineral organization.

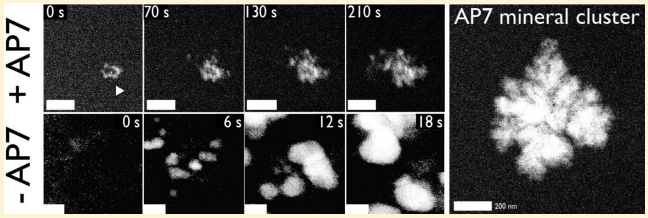

The biomineralization process in the mollusk shell is a complex bioengineering feat that leads to the formation of oriented, dimensionally controlled calcium carbonate mineral polymorphs of either calcite, aragonite, or both.[1−7] Of importance to this shell engineering process is the formation of the organic extracellular matrix (ECM), which oversees the mineralization process and tailors the formation of the prismatic (calcite) and/or nacre (aragonite) shell layers for the survival of each mollusk species.[8,9] To date, more than 50 different molluscan ECM prismatic and nacre protein genes have been identified, which indicates just how complex the shell formation process may be.[8−14] An important subset of these proteins, known as the intracrystalline proteome,[15−20] are found as occluded species within nacre aragonite tablets. The other protein subset, known as the framework proteome, is associated with the β chitin−silk gel phase that coats the outer regions of the aragonite tablets.[8,12,13] Together, both proteomes participate in aragonite tablet formation and contribute to the fracture toughening properties of the nacre.[8,12,13,15−20] To understand this outcome, we need to determine framework and intracrystalline proteome involvement within the early events in the nucleation process and in subsequent postnucleation events leading up to incorporation of protein within the mineral phase. Unfortunately, this information is not yet available, and as a result, our present understanding of the mollusk shell biomineralization process and our ability to harness it for materials applications are very limited.

In the nacre layer of the Pacific red abalone gastropod (*Haliotis rufescens*), there exists a group of intracrystalline proteins known as the AP proteome.[15,16] The most studied AP protein is AP7 (66 amino acids, 7565 Da),[15] a non-phosphorylated, nonglycosylated member of the Zn(II) binding C-RING superfamily of proteins that are associated with protein−protein interaction and intracellular signaling.[21,22] Within *in vitro* settings (carbonate vapor diffusion experiments), AP7 is known to inhibit calcite formation and forms lamellar and clustered single-crystal aragonite.[21,22] However, the efficiency of AP7 in stabilizing aragonite *in vitro* is low, and the process requires high protein concentrations (i.e., 100 μM).[21] This suggests that AP7 may not function as a true aragonite stabilizer *in vivo* but perhaps plays other important

Received: July 18, 2014
Revised: September 23, 2014
Published: October 29, 2014

   dx.doi.org/10.1021/bi5008854 | *Biochemistry* 2014, 53, 7259−7268

roles related to nacre tablet formation. Structurally, the AP7 protein consists of residually structured (C-terminal) and intrinsically disordered (N-terminal) regions (Supporting Information, Figure S1).[21−23] Intrinsic disorder, or the absence of internal stabilization and presence of unfolded structure(s) in protein sequences, is an important asset for protein−protein interaction and promoting internal protein mobility. AP7 also possesses three amyloid-like aggregation-prone cross-β strand domains (Supporting Information, Figure S1), two of which are found within the C-terminal domain.[24] Under mineralization conditions, this interesting combination of disordered and aggregation-prone sequence features leads to the formation of AP7 assemblies that contain mineral deposits[22] and introduce organized nanomineral deposits and subsurface nanoporosities into calcium carbonate crystals.[25] We note that protein oligomerization or aggregation has been documented for other aragonite-associated proteins,[26−29] so the self-associative behavior of AP7 is significant. However, the details of the AP7 oligomerization process and its relevance to pre- and postnucleation events in the nonclassical nucleation pathway[30−37] are not known. Thus, our understanding of the participation of intracrystalline proteins in nacre tablet formation, organization, and occlusion is largely incomplete.

To address these shortcomings, we present a new study that integrates biophysical and *in situ* experiments to clarify both the AP7 protein oligomerization process and the participation of these assemblies in prenucleation and postnucleation events. We find that AP7 spontaneously forms phases (oligomers and films) in solution and these phases undergo further oligomerization in the presence of Ca^{2+} and mineral assay solutions, similar to the agglomeration behavior observed for other nacre proteins.[26,28] Using nuclear magnetic resonance (NMR) spectroscopy, we find that the protein phases are stabilized by C-RING−C-RING domain interactions[22] yet destabilized to a certain extent by the intrinsically disordered D1−T19 N-terminal sequence, and thus, the AP7 phases appear to be amorphous and mobile under solution conditions. Using potentiometric titration methods,[30−35] we determine that AP7 phases do not affect ACC formation or stability but do influence early nucleation events by extending the time intervals for PNC formation relative to the control scenarios. Finally, time-resolved *in situ* flow cell scanning transmission electron microscopy (STEM) mineralization studies confirm that AP7 phases delay the onset of nucleation and assemble and organize mineral nanoparticles into ringlike or branching clusters, thereby mirroring a similar process that occurs when these same protein phases organize mineral nanoparticles on calcite surfaces.[25] Collectively, these results demonstrate that disordered, aggregation-prone intracrystalline proteins such as AP7 form protein phases that influence early nucleation events[30−35] and establish strategic associations with the forming mineral phase that lead to mineral organization.

EXPERIMENTAL PROCEDURES

Chemical Synthesis, Recombinant Expression, and Purification of AP7. Chemically synthesized AP7 (cAP7) was obtained and purified as described in previous reports.[21,22] In experiments that utilized cAP7, the protein solutions were prepared by dissolving the appropriate amount of lyophilized cAP7 directly into the required buffer solutions. For heteronuclear $^{13}C-^{15}N$ NMR experiments with AP7 oligomers, the gene synthesis, cloning, bacterial expression, and purification (94%) of uniformly labeled $^{13}C/^{15}N$ recombinant AP7 (rAP7, 67 amino acids, His tag-free, with a Gly residue occupying position 1 at the N-terminus after TEV protease cleavage of the Trx-His_6-TEV-AP7 fusion protein) were performed by GenScript USA (Piscataway, NJ) using their proprietary OptimumGene system and Bio-Express Cell Growth Media [U-^{13}C, 98%; U-^{15}N, 98% (Cambridge Isotope Laboratories, Andover, MA)].[26−28] An advantage of using the thioredoxin (Trx) tag in rAP7 expression is the antioxidant protection that Trx affords against unwanted oxidation of AP7 Cys thiol groups during expression and purification. The extent of double labeling was verified to be 98.9% using ESI-MS TOF. The purified, free thiol cAP7 and rAP7 proteins were subsequently dissolved in H_2/N_2-flushed unbuffered deionized distilled water (UDDW).[11,15,16] Aliquots were then stored at −20 °C in airtight sealed vials that were preflushed with high-purity N_2 gas to avoid disulfide bond formation and/or thiol oxidation during storage. For subsequent NMR experimentation, rAP7 samples were created by exchanging and concentrating appropriate volumes of the protein stock solution into the appropriate buffer using Amicon Ultra 0.5 ultrafiltration concentrators (3 kDa molecular weight cutoff, Millipore Corp.) and determining the final protein concentration via absorption spectrophotometry at 230 nm.

Atomic Force Microscopy (AFM) Imaging of AP7 Assemblies. We investigated the dimensional and morphological characteristics of AP7 assemblies captured from solution onto mica substrates. The following samples were investigated. cAP7 samples (380 nM and 1.3, 5, and 13.3 μM) were imaged in 10 mM Tris-HCl, pH 8.0 buffer. In the case of the 380 nM and 5 μM samples, additional imaging was performed in 10 mM Tris-HCl and 10 mM $CaCl_2$ (pH 8.0). Note that imaging of Ca^{2+} samples utilized Tris-HCl as the buffering species instead of carbonate or bicarbonate, because carbonate ions will combine with Ca^{2+} ions and form inorganic precipitates that make protein complex detection and interpretation difficult to achieve via AFM. The rAP7 NMR sample (see below) was imaged at a protein concentration of 33 μM in UDDW (pH 7.5). For comparison with our potentiometric experiments, a parallel 1.3 μM cAP7 sample was imaged at pH 9.0 in 10 mM glycine instead of Tris-HCl or carbonate/bicarbonate buffers because Tris exhibits poor buffering capacity at pH 9.0 and carbonate/bicarbonate buffers in the open AFM cell are prone to pH drift.

AFM experiments were conducted at 25 °C using an Asylum MFP-3D atomic force microscope operating in tapping mode in a buffer solution.[26,28] V-Shaped Si_3N_4 cantilevers (reported spring constant of 0.09 N/m) were used for imaging. A precise drive frequency in fluid (~9 kHz) was calculated for each cantilever prior to imaging by overlaying the thermal spectrum over the frequency sweep. All samples were aliquoted onto a freshly stripped surface of mica (0.9 mm thick, Ted Pella, Inc.) and incubated for a period of 15 min at ambient temperature prior to measurement. Igor Pro version 6.01 (http://www.wavemetrics.com) was used for image acquisition at a scan rate of 2 Hz. Gwyddion was implemented for image processing, noise filtering, and analysis, including the calculation of R_q, i.e., surface roughness of the imaging surface.[26,28]

NMR Spectroscopy. Lyophilized rAP7 was dissolved in UDDW containing 10% (v/v) D_2O (99.99 atom % D, Cambridge Isotope Laboratories), and the pH was adjusted to 7.5 using microliter volumes of NaOH. Note that base-catalyzed amide backbone exchange kinetics at pH ≥8.0 prevents the collection of interpretable NMR data for rAP7

dx.doi.org/10.1021/bi5008854 | *Biochemistry* 2014, 53, 7259−7268

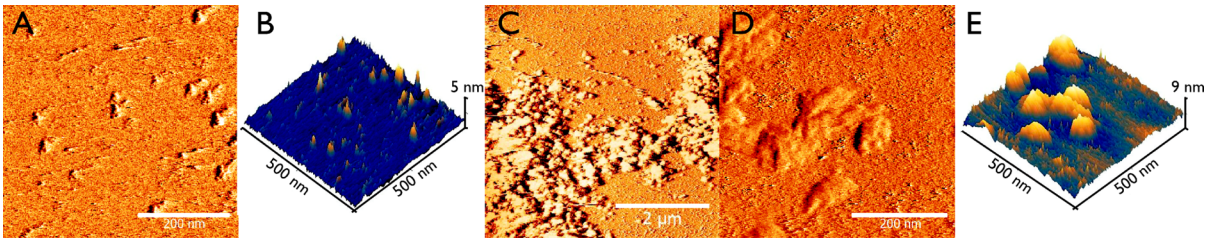

Figure 1. Tapping mode AFM images of 5 μM AP7 on freshly cleaved mica. (A) Apo state in 10 mM Tris-HCl (pH 8.0). Note the presence of round-to-angular features in the apo oligomers. (B) *z* plot of the region depicted in panel A. (C) In the presence of 10 mM Tris-HCl and 10 mM $CaCl_2$ (pH 8.0). (D) Enlargement of the peripheral area depicted in panel C. (E) *z* plot of the region depicted in panel D.

under mineralization conditions. Thus, we performed experiments at pH 7.5, which is close to the assay pH of 8.0 and permits maximal detection of exchangeable backbone and side chain N−H spin systems. The final protein concentration was 33 μM. Under these conditions, AP7 forms a soluble protein phase or aggregate that does not precipitate out as evidenced by the absence of detectable turbidity at 380 nm and confirmed by AFM imaging on freshly cleaved mica (Supporting Information, Figure S2). Samples were loaded into 5 mm symmetrical D_2O-matched Shigemi NMR microtubes (Shigemi, Inc., Alison Park, PA). Periodic ^{15}N HSQC experiments were conducted to verify that decreased signal intensities or line width broadening associated with precipitation did not occur. The rAP7 ^1H NMR spectra were compared to the cAP7 ^1H NMR spectra acquired in a previous study[22] and found to be nearly identical (data not shown). $^1H-^{15}N$ and $^1H-^{13}C$ HSQC NMR experiments were conducted on rAP7 at 25 °C using a Bruker AVANCE 800 MHz spectrometer equipped with a four-channel 5 mm cryoprobe. Bruker TOPSPIN was used to process all data. The spectra were referenced with respect to the temperature-corrected water resonance, and ^{13}C, ^{15}N, and ^1H chemical shifts were referenced on the basis of the IUPAC guidelines using the unified chemical shift scale.[38] Secondary structure estimates for select HSQC spin systems (Gly and Thr) were determined using $^{15}N_\alpha$, $^{13}C_\alpha$ protein database chemical shift referencing.[38−40]

Potentiometric Ca^{2+} Titration. Potentiometric titration experiments were performed at room temperature by using a computer-controlled titration system operated with the supplied software (Tiamo version 2.2, Metrohm GmbH, Filderstadt, Germany). The experimental setup has been described previously.[30−35] A polymer-based ion-selective electrode and a flat-membrane glass electrode were used to monitor the free Ca^{2+} concentration and pH, respectively. During a titration run, a $CaCl_2$ (10 mM) solution was dosed at a constant rate of 0.01 mL/min to 10 mL of the protein solution in carbonate buffer (10 mM), which was constantly stirred at 800 rpm and room temperature. Parallel runs were conducted on 1.3 and 13.3 μM cAP7 samples. Titrations were performed at a constant pH value of 9.0 that were maintained by countertitration of NaOH (10 mM). Reference and calibration experiments were performed by dosing $CaCl_2$ (10 mM) into carbonate buffer (10 mM, pH 9.0) and water (pH 9.0), respectively.[30−35]

STEM Liquid Flow Cell Imaging of Mineralization. To monitor the dynamics of formation of the protein−mineral complex, fluid cell scanning transmission electron microscopy experiments were performed using a three-port Poseidon 200 liquid flow cell holder (Protochips, Inc.) in an aberration-corrected JEOL 2200 FS instrument. The microscope was operated in scanning transmission electron microscopy (STEM) mode with spot size 3C at 200 kV using a high-angle annular dark-field (HAADF) detector. The calcium- and carbonate-containing assay solutions for both protein-containing and protein-deficient assay were prepared from 20 mM $CaCl_2{\cdot}2H_2O$ and 20 mM $NaHCO_3$, respectively (the final assay solution being a 1:1 mixture; the final pH being 8.1−8.3).[25,28,29] In protein experiments, a final assay concentration of 13.3 μM cAP7 was utilized. For the mixing experiment, 500 nm spacers and flow rates between 90 and 180 μL/h were used. The TEM holder was first flushed with the cAP7/carbonate solution, and STEM imaging was performed to confirm that no precipitation took place in the absence of the calcium solution. Once injection of the calcium solution had been initiated through the second inlet port, continuous imaging was performed. We repeated this experiment once to control the reproducibility and found a similar precipitation behavior in both cases.

RESULTS

In this study, we utilized two different forms of AP7. The chemically synthesized version (95% pure), which has been the subject of previous studies,[21,22,25] was used in all experiments except for the NMR studies, where the uniformly labeled $^{13}C/^{15}N$ recombinant His tag-free form (rAP7, 67 amino acids, Gly at position 1, 94% pure) was employed at higher protein concentrations required for NMR sensitivity (i.e., 33 μM). Both forms of the protein oligomerize to form phases (Supporting Information, Figure S2). Note that AP7 is oligomeric over the pH range of 4−9,[22] which encompasses the pH ranges utilized in our AFM, NMR, STEM, and potentiometric experiments.

AP7 Spontaneously Forms Oligomeric Particles and Films on Mica Surfaces. Previously, AP7 self-association was studied as a function of pH using dynamic light scattering (DLS).[22] Understandably, these studies required the use of filtration, and thus, any >0.2 μm protein oligomers, not to mention protein films, would have evaded analyses. Thus, we utilized tapping mode AFM imaging to more definitively monitor apo-AP7 (i.e., calcium-free) oligomerization at pH 8, which corresponds to the pH range for most *in vitro* calcium carbonate mineralization assays (Figure 1).[21−23] Here, we observe apo-AP7 oligomerization over the protein concentration range of 1.3−33 μM (Supporting Information, Figure S2). In general, apo-AP7 oligomers present on mica surfaces as nanometer-sized particles that possess rounded to angular morphologies, which are readily seen at 5 μM (Figure 1A,B). These angular features were not caused by tip artifacts as evidenced by parallel imaging on two other nacre proteins, n16.3[28] and PFMG1,[26] using the same tips and AFM instrument (Supporting Information, Figure S3). The AP7 oligomers are mobile and sometimes translate on mica surfaces

dx.doi.org/10.1021/bi5008854 | *Biochemistry* 2014, 53, 7259−7268

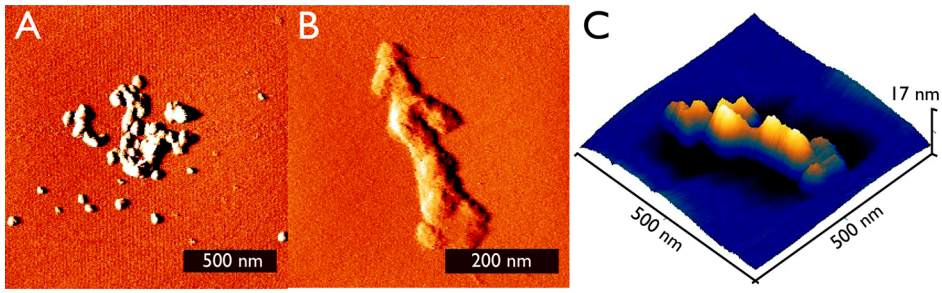

Figure 2. (A) Tapping mode AFM amplitude image of 380 nM AP7 on freshly cleaved mica in the presence of Ca^{2+} [10 mM Tris-HCl and 10 mM $CaCl_2$ (pH 8.0)]. (B) Higher-magnification amplitude image taken of a select region in panel A, showing round-to-angular morphologies. (C) *z* plot corresponding to the amplitude image depicted in panel B.

at a frequency faster than that of tapping mode detection. As a result, these mobile oligomers often feature elongated morphologies (Figure 1A) that are more clearly observed at 5 μM AP7 (because of oligomer mobilities, we did not calculate particle diameters or heights at this time). A comparison of surface roughness values [R_q (see Experimental Procedures)] obtained for freshly cleaved mica surfaces in buffer (R_q = 0.078 nm) versus mica surfaces exposed to 5 μM apo-AP7 in the same buffer [R_q = 0.15 nm, a ~2-fold increase (Figure 1A,B)] indicates that a protein coating or film exists on the mica surface.[26,28] From this, we conclude that AP7 exists as a two-component phase of protein films and amorphous oligomers on mica surfaces, similar to the findings obtained for the Japanese pearl oyster framework nacre protein, n16.3,[28] and the pearl protein, PFMG1.[26] Henceforth, we will collectively refer to AP7 oligomer films as AP7 "protein phases".

Published dynamic light scattering (DLS) studies indicated that the introduction of Ca^{2+} significantly increases AP7 oligomer dimensions.[22] To be consistent with these studies, and to avoid misinterpretations of amorphous mineral particles and protein oligomer identities, we elected to image AP7 in the presence of Ca^{2+} but in the absence of carbonate and/or bicarbonate species. As shown in Figure 1C–E, Ca^{2+} induces significant aggregation of AP7, leading to the formation of clustered amorphous protein phases on mica surfaces (Figure 1C). The dimensional increases were so significant that we encountered sample thickness and AFM tip positioning issues. Thus, we were able to image only the peripheral regions (Figure 1D,E) of the overall aggregate. In addition, we measured an R_q value of 0.82 nm for the 10 mM Ca^{2+}/5 μM AP7 sample, and this value represents a 5-fold increase and a 10-fold increase over values obtained for apo-AP7 and freshly cleaved mica, respectively (see above). This increase in surface roughness also confirms that AP7 film formation has been enhanced by the addition of Ca^{2+}.

Given the extraordinary increase in AP7 phases in the presence of Ca^{2+} (Figure 1B), we also imaged a more dilute AP7 sample (380 nM) (Figure 2A–C). Although apo-AP7 oligomers were not detected at this low concentration (data not shown), in the presence of Ca^{2+} we do observe individual and clustered AP7 oligomers on the mica surface (Figure 2A). In most cases, the oligomers feature similar round-to-angular morphologies (Figure 2B) that we initially observed for 5 μM apo-AP7 (Figure 1A). We conclude that Ca^{2+} or electrostatic screening[41,42] induces significant aggregation or clustering of AP7 phases on mica surfaces compared to that seen under apo conditions.

Oligomeric AP7 Possesses Labile, Disordered Protein Domains. Previously, homonuclear ^{1}H NMR spectroscopy revealed that not all of the amino acid residues in oligomeric apo-AP7 are involved in intermolecular contacts.[22] This suggests that AP7 protein molecules within assemblies possess protein backbone regions that are unrestrained and more labile or unstable compared to sequence regions involved in protein–protein contact. If true, then this molecular instability may explain why apo-AP7 oligomers appear to be amorphous and heterogeneous in dimension (Figure 1A,B). However, previous homonuclear NMR experiments failed to identify the location of these labile sequences and thus could not explain the nature of this instability.[22] To address this issue, we performed multidimensional ^{15}N- and ^{13}C-edited HSQC NMR experiments on uniformly ^{13}C- and ^{15}N-labeled apo-rAP7 phases at pH 7.5 (Figure 3). As expected, intermolecular contacts between protein molecules lead to the attenuation of the majority of backbone and side chain ^{13}C–^{15}N HSQC resonances for this sample. The loss or broadening of NMR signals was also observed in aggregation studies involving other biomineralization proteins.[43−46] The attenuation of NMR cross-peaks reflects aggregation-induced changes in backbone dynamics, intermediate time scale broadening, and signal intensity attenuation of the HSQC resonances that are involved in intermolecular contacts.[43−46]

However, a closer look at the HSQC spectra reveals that not all of the rAP7 NMR resonances are fully attenuated or involved in intermolecular contacts. We detected a limited number of ^{1}H and ^{15}N backbone and ^{1}H, ^{15}N, and ^{13}C side chain resonances in the HSQC spectra (Figure 3) that are consistent with the presence of labile or unrestrained sequence regions[43−46] within assembled rAP7 protein molecules. Although NMR signal attenuation prevents us from obtaining sequence-specific spectral assignments for observable cross-peaks at this time, we can leverage some of the unique sequence features of this protein to estimate the location of detectable residues within the rAP7 sequence and establish the nature of this polypeptide instability. One unique feature in the rAP7 sequence is the presence of six Gly residues [recombinant positions 1, 5, 8, 10, 18, and 53 (Figure 3)]. Gly is readily distinguishable on the basis of ^{1}H, ^{13}C, and ^{15}N chemical shifts[38,47] and is a significant component of intrinsically disordered sequences.[48−51] An examination of the HSQC spectra reveals the presence of Gly α-NH (Figure 3A) and α-CH backbone-specific cross-peaks (Figure 3B). These Gly backbone $^{15}N_\alpha$ and $^{13}C_\alpha$ cross-peaks resonate at 110–108 and 43.5 ppm, respectively, and we note that these values are within ±1 ppm for corresponding random coil Gly $^{15}N_\alpha$ and $^{13}C_\alpha$

dx.doi.org/10.1021/bi5008854 | *Biochemistry* 2014, 53, 7259–7268

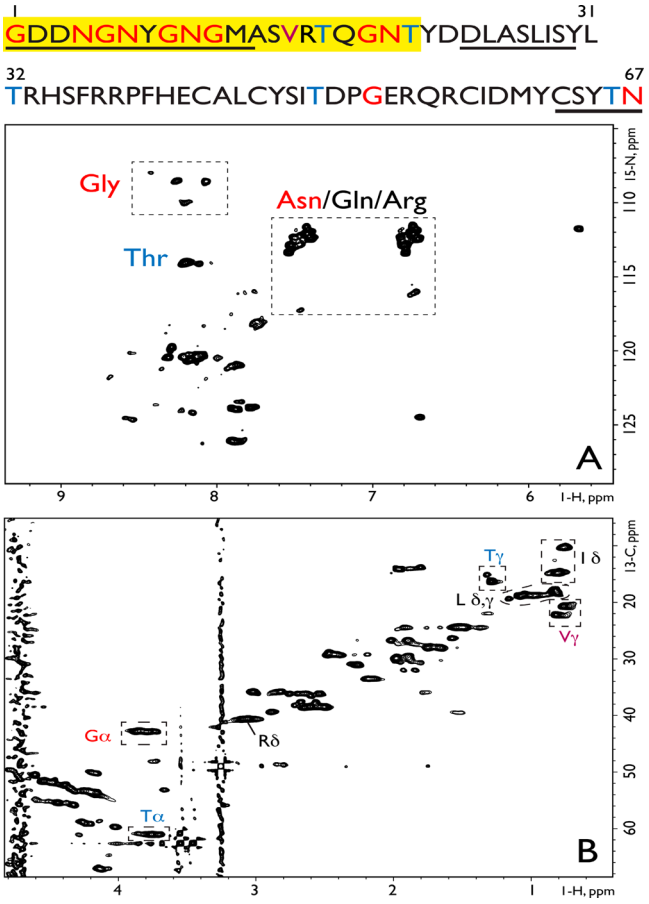

Figure 3. (A) ^{15}N- and (B) ^{13}C-edited HSQC NMR spectra of 33 μM rAP7 in UDDW (pH 7.5). Tentative assignments of side chain and backbone spin systems are shown in each spectrum. For evaluation, the primary sequence of the 67-amino acid rAP7 sequence is presented, using the numbering system that accounts for the N-terminal Gly residue (G1) that remains after TEV protease cleavage. The locations of predicted intrinsically disordered sequences are underlined (see also the Supporting Information), and the labile, disordered region identified by the HSQC experiments is highlighted in yellow. For the sake of identification, color coding of Gly (red), Asn (red), Val (purple), and Thr (blue) residues is provided on the spectra and in the sequence. In panel B, note that other side chain ^{13}C spin systems were identified on the basis of their distinctive methyl and methylene ^{13}C chemical shift distributions, and these include Ile, Leu, and Arg. Unfortunately, because these amino acids occur in both the N- and C-terminal regions of the AP7 sequence, we are unable to pinpoint their locations at this time.

chemical shifts.[38−40] Hence, there is a high probability that these Gly residues reside within intrinsically disordered regions of rAP7 protein molecules. Along with Gly, we also note the presence of ^{15}N side chain amide HSQC cross-peaks that are characteristic for another common structural disruptor, Asn (Figure 3A).[48−51] Interestingly, five of the six Gly residues are located within the 30-amino acid N-terminal sequence, and, four of the five Asn residues are partnered with Gly in -NG- or -GN- dipeptide blocks in this same region (Figure 3). Thus, we conclude that the observable Gly ^{1}H, ^{15}N, and ^{13}C and Asn ^{1}H and ^{15}N HSQC cross-peaks represent the remnant G1 residue and N4−N6, G8−G10, and G18−N19 segments of the intrinsically disordered N-terminal domain[52] of rAP7 (Figure 3, target residues colored red using the numbering system for the modified rAP7 sequence). Note that the -NG- rich C-terminal T64−W98 sequence was also found to be disordered and unrestrained with nacre framework n16.3 protein phases under similar conditions.[28]

Two other findings also implicate the AP7 N-terminal domain as a random coil disordered sequence lacking intermolecular stabilization within protein assemblies: (a) the appearance of Val γ-CH_3 side chain cross-peaks in the ^{1}H−^{13}C HSQC spectrum (Figure 3B) (note that Val occurs only at position 14 in rAP7 where it is flanked both upstream and downstream by the disordered G8−G10 and G18−N19 dipeptide blocks) and (b) the presence of Thr $^{15}N_{\alpha}$, $^{13}C_{\alpha}$ backbone and γ-$^{13}CH_3$ side chain cross-peaks (Figure 3A,B). Note that two of the four Thr residues (T16 and T20) in the rAP7 sequence flank either side of the labile G18−N19 dipeptide sequence. The observed $^{15}N_{\alpha}$ and $^{13}C_{\alpha}$ chemical shifts for these Thr HSQC cross-peaks resonate at 114 and 61 ppm, respectively, which are within 1−2 ppm of the Thr random coil values ($^{15}N_{\alpha}$ = 116−114 ppm; $^{13}C_{\alpha}$ = 61−62 ppm)[38−40] and thus are consistent with the location of these Thr residues within an unstructured region. Thus, our experiments confirm that the unstable region observed in our HSQC spectra encompasses the G1−T20 sequence in rAP7 (Figure 3, yellow highlighted region), which would correspond to the D1−T19 sequence in the native protein (Supporting Information, Figure S1). Note that earlier NMR studies established the presence of random coil conformation within a model peptide representing N-terminal amino acids 1−30 of the AP7 sequence,[52] so it is possible that this disordered, unstable region may extend beyond T19 in the assembled native AP7 protein molecules.

In conclusion, we deduce that the N-terminal segment containing -NG- and -GN- [D1−T19 in the native sequence (Supporting Information, Figure S1)] exists as an unrestrained, disordered random coil region within aggregated AP7 protein molecules. Conversely, the aggregation-prone T31−N66 C-RING domain[22] (Supporting Information, Figure S1) is most likely involved in intermolecular contacts between AP7 molecules based upon the following evidence. (a) We are unable to detect C-terminally associated HSQC cross-peaks for the protein phase sample (Figure 3), and (b) the AP7 T31−N66 C-RING sequence possesses two aggregation-prone cross-β strand regions[24] and is known to be strongly self-associative[22] (Supporting Information, Figure S1). Thus, AP7 phases are stabilized by C-RING−C-RING domain interactions[22] yet destabilized to a certain extent by the intrinsically disordered D1−T19 N-terminal sequence. The destabilizing nature of the N-terminal sequence most likely leads to the amorphous morphologies and heterogeneous dimensions that we observe for AP7 phases (Figure 1A,B).

AP7 Protein Phases Alter Prenucleation Cluster (PNC) Formation and Kinetics. It is known that *in vitro* calcium carbonate mineralization can be described by a nonclassical nucleation scheme that involves the initial formation of nanometer-sized PNCs that assemble into larger clusters of amorphous calcium carbonate (ACC).[3,4,30−35] These ACC clusters can be temporally stabilized or undergo transformation into the crystalline phase.[30−37] With this in mind, we wished to address the role of intracrystalline AP7 protein phases in this nonclassical nucleation process. To do this, we utilized potentiometric experiments[30−35] to monitor early nucleation events in the presence of AP7 alongside reference experiments [i.e., protein-deficient (Figure 4 and Table 1)] at pH 9.0. Note that AP7 is oligomeric at pH 9.0 as confirmed by tapping mode

dx.doi.org/10.1021/bi5008854 | *Biochemistry* 2014, 53, 7259−7268

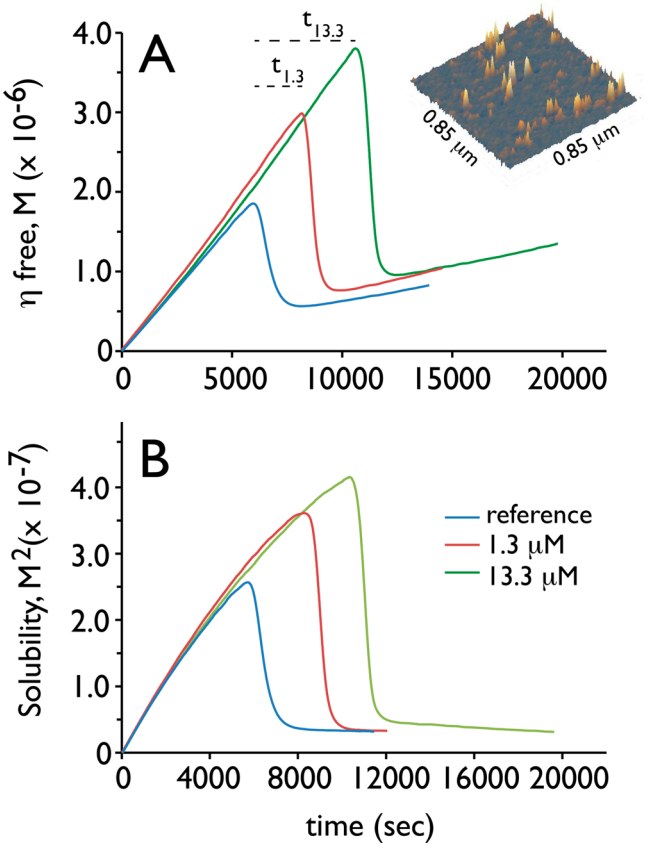

Figure 4. Potentiometric Ca^{2+} titrations of 1.3 and 13.3 μM AP7 in 10 mM carbonate buffer (pH 9.0) as a function of time. In each plot, the reference curve refers to parallel experiments conducted in the absence of protein. In panel A, the plot represents the time interval (t) required for nucleation of the initially formed calcium carbonate phase, denoted as η_{free}. For the sake of clarity, above each curve in panel A we have marked the time intervals ($t_{1.3}$ and $t_{13.3}$) for each AP7 concentration relative to the reference experiment. In panel B, the plot represents the solubility or stability of the forming ACC phase. The inset in panel A is an AFM tapping mode z plot image (maximum z axis height of 1.6 nm) for a 1.3 μM AP7 sample (pH 9.0) in 10 mM glycine buffer, which confirms the presence of oligomer particles at this pH [compare this AFM image to that obtained for 5 μM AP7 at pH 8 (Figure 1)]. Note that for the pH 9.0 imaging experiments, Tris exhibits poor buffering capacity and carbonate/bicarbonate buffers in the open AFM cell are prone to pH drift. Hence, we utilized glycine to minimize pH drift issues.

Table 1. Ca^{2+} Potentiometric Titration Data Obtained for cAP7 and Reference (protein-deficient) Samples

sample	pH	NT[a] (s)	slope[b] (mol/s^2)	solubility (M^2)[c]
reference	9	5975	3.21×10^{-10}	3.16×10^{-8}
1.3 μM	9	8160	3.43×10^{-10}	3.28×10^{-8}
13.3 μM	9	10600	3.40×10^{-10}	3.14×10^{-8}

[a]Nucleation time. [b]Prenucleation slope. [c]Postnucleation solubility.

AFM (Figure 4, inset). We alert the reader that potentiometric titrations performed below pH 9.0 tend to be problematic in that bicarbonate dominates by far and the carbonate ion is almost nonexistent, making pH control difficult.[30−35] Thus, performing potentiometric Ca(II) titrations with nacre proteins at pH 9.0 leads to more reproducible results.

The standard potentiometric curve (Figure 4A) provides information about the formation and stabilities of PNCs in solution. As free Ca^{2+} is added to the carbonate solution, ion complexes (i.e., PNCs) form, and this is represented by the initial linear region of the titration curve. Where the measured level of free Ca^{2+} decreases upon further addition of $CaCl_2$ (i.e., the peak region), this marks the start of solid phase nucleation (e.g., ACC) from PNCs.[30−35] As shown in Figure 4A and Table 1, the time interval (t) or difference between AP7 and reference peak regions was significantly altered by AP7 phases at pH 9.0. This time interval difference can be quantitated by a scaling or retarding factor (F), which is the quotient of the average nucleation time in the presence of the agent and that of the respective NaCl reference[53] and quantifies the nucleation inhibition. At pH 9.0, the calculated F values are 1.3 and 1.8 at AP7 concentrations of 1.3 and 13.3 μM, respectively. Hence, AP7 phases prolong the time interval for PNC formation before nucleation, with the maximal effect being nearly a factor of 2 greater (at 13.3 μM) than that of the reference state. With respect to PNC stability, the slope of the prenucleation regime (i.e., the initial linear region) provides indirect evidence of the interaction between additive molecules and solute ion associates, leading to PNC stabilization (i.e., $slope_{additive} < slope_{ref}$) or destabilization ($slope_{additive} > slope_{ref}$).[30−35] As shown in Table 1, the slope of the prenucleation regime in the presence of AP7 did not differ significantly with respect to the reference titration curve. Thus, AP7 does not affect the calcium carbonate prenucleation cluster equilibrium; i.e., AP7 phases neither stabilize nor destabilize PNC clusters.

With regard to the formation and stability of ACC, this information can be extracted from the free Ca^{2+} titration (Figure 4A) and the postnucleation solubility (Figure 4B) curves. In Figure 4A, the formation of ACC commences at the peak value and the subsequent sigmoidal curve region traces the ACC formation process.[30−35] Here, we note that the end points for the AP7 and reference sigmoidal curves are similar, and thus, AP7 phases do not significantly influence ACC formation relative to the reference state. Interestingly, no detectable Ca^{2+}−AP7 binding was observed in any of the titration curves, which supports our earlier findings that AP7 does not exhibit high affinity for Ca^{2+}.[21,22] With regard to postnucleation solubility or the stability of the ACC phase (Table 1 and Figure 4B), we observe that the solubilities of the initial mineral deposits remain relatively constant in the presence and absence of AP7 (i.e., the slopes and end points are the same). The solubility values indicate that prevaterite and precalcite ACC are the initial nucleated products in our systems as reported previously.[53,54] In conclusion, although AP7 phases prolong the time interval for PNC formation, they do not significantly impact the ACC formation process and neither stabilize nor destabilize ACC clusters or PNCs.[53,54]

Evidence of AP7 Protein Phases Capturing and Assembling Mineral Nanoparticles. Previously, vapor diffusion assay experiments conducted with AP7 verified the association of mineral particles with the protein phase.[22] However, these studies suffered from three shortcomings. First, vapor diffusion assays cannot precisely control carbonate content, which limits reproducibility.[25,28,29] Second, the need for a >10 h nucleation time scale prevented direct assessment of early nucleation events (i.e., <15 min) that potentially overlap with spontaneous protein oligomerization. Third, sample dehydration in TEM can distort AP7 protein phase−mineral associations. To resolve this, we employed liquid flow cell STEM imaging to directly examine early events in the nucleation process in solution (Figures 5 and 6) at protein

dx.doi.org/10.1021/bi5008854 | Biochemistry 2014, 53, 7259−7268

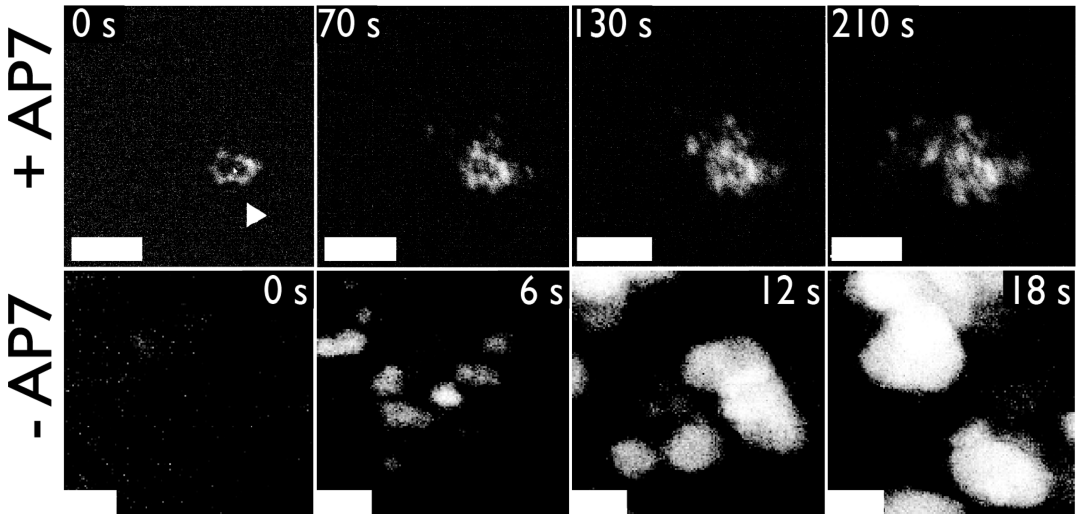

Figure 5. STEM video stills of mineral nanodeposits forming in calcium carbonate solutions in the presence and absence of 13.3 μM AP7. For AP7 experiments, the sequence of images starts 45 min after injection of the calcium solution (first frame, denoted as 0 s) when mineral nanodeposits are first detected (white arrow, first frame) and nucleation evolves slowly (i.e., 210 s). Note the formation of ringlike nanoclusters as time evolves. By comparison, in the protein-deficient experiments, mineral nanodeposits are first observed 20 min after injection (first frame, denoted at 0 s) of the calcium solution and evolves much more rapidly and without organization. For (+) AP7 images, scale bars are 100 nm; for (−) AP7 images, scale bars are 50 nm. A more comprehensive series of video stills (Figures S4 and S5) and the videos themselves (Movies S1 and S2) can be found in the Supporting Information. Qualitative evidence of calcite formation during this process is presented in Figure S6 of the Supporting Information.

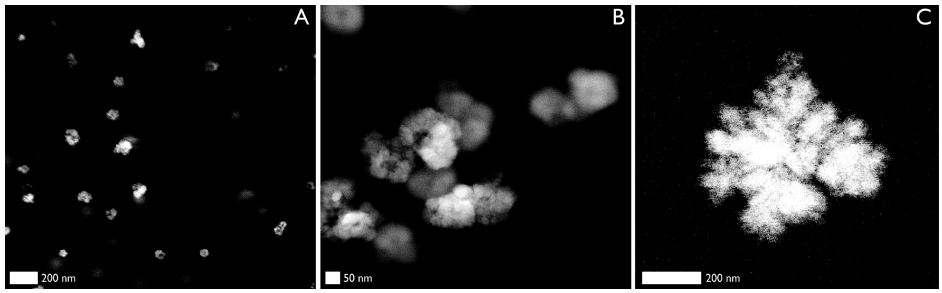

Figure 6. STEM video stills of representative AP7-induced mineral ringlike cluster ensembles that form from calcium carbonate solutions. Images were captured 60 s after the first evidence of mineral nanodeposit formation was noted. Note the ringlike structures in panel B and the internal branching morphology in panel C.

concentrations that are commensurate with those utilized in our potentiometric studies [i.e., 13.3 μM (Figure 4)]. Note that STEM flow cell experimental considerations necessitated mineral assay conditions [$CaCl_2$/$NaHCO_3$ (pH 8.1−8.3) (see Experimental Procedures)] different from those employed in the potentiometric study [$CaCl_2$/Na_2CO_3 (pH 9)]. Nonetheless, STEM imaging is particularly sensitive to atomic mass, and thus, we can directly observe the formation and organization of Ca rich mineral nanoparticles in solution and monitor amorphous-to-crystalline transformation induced by electron beam irradiation.

At 20 min postmixing, the first electron dense round mineral nanoparticles are observed in the protein-deficient assays and rapid mineralization occurs over a 23 s interval without evidence of organization (Figure 5; Supporting Information, Figures S3 and S4 and Movie S1). In contrast, at 45 min postmixing, the first mineral nanoparticles are observed in the AP7 assays and thus the time interval for nucleation is prolonged by a factor of at least 2 in the presence of the protein phases (Figure 5; Supporting Information, Figure S4 and Movie S2). This is in agreement with our potentiometric titration findings (Figure 4 and Table 1). In both assays, we determined that the mineral nanoparticle formation was not in response to electron irradiation because these species also occurred in areas that had previously not been exposed to the electron beam (data not shown). What is most striking about the STEM assays is that mineral nanoparticles agglomerate or organize in the presence of AP7 but not in the protein-deficient assays (Figures 5 and 6; Supporting Information, Figures S4 and S5 and Movies S1 and S2). This AP7-driven agglomeration process led to the formation of ring-shaped clusters that continued to grow by further attachment of mineral nanoparticles as time evolves (Figures 5 and 6). The ringlike structures suggest that the AP7 protein phases are organizing the mineral nanoparticles. This organizational capability is further supported by two other pieces of evidence: (a) the presence of branching morphologies in the assembled clusters (Figure 5), which most likely reflects the positioning of individual nanoparticles that were assembled from solution by the protein phase, and (b) previous TEM studies that showed that AP7 phases rescued from mineralization assays feature a branching morphology and associate with mineral nanoparticles.[22] Hence, we conclude that AP7 phases are promoting mineral nanoparticle clustering and organization. Because of the limitations of STEM flow cell imaging, we are unable to fully characterize the mineral phases that form in our assays in terms

dx.doi.org/10.1021/bi5008854 | *Biochemistry* 2014, 53, 7259−7268

of crystallinity and lattice structure, although qualitative estimates of facet angles in images obtained at later stages of nucleation suggest that calcite, not aragonite or vaterite, is forming in the AP7 assays (Supporting Information, Figure S6). Nonetheless, we conclude that AP7 phases have a significant impact on the mineralization process in solution by prolonging the time interval for PNC formation (Figure 4) and assembling and organizing mineral nanoparticles in solution (Figures 5 and 6).

DISCUSSION

Using a combination of biophysical and *in situ* techniques, we have identified the participation of an intracrystalline protein phase within the nonclassical nucleation pathway[30−37] and the subsequent postnucleation process of mineral organization. We find that AP7 phases perform two *in vitro* mineralization functions. First, AP7 delays the onset of mineral nucleation and prolongs the time interval for PNC formation yet does not appreciably affect PNC stabilities or ACC formation or stability (Figure 4 and Table 1). Thus, AP7 phases are tuned to respond to very early aspects of mineral nucleation in solution (i.e., PNC formation). Second, we observe that AP7 phases agglomerate and organize mineral nanoparticles from solution (Figures 5 and 6; Supporting Information, Figures S4−S6 and Movies S1 and S2). This solution-based mineral assembly process also mirrors a similar phenomenon that occurs when AP7 protein phases contact calcite crystals and organize clustered mineral nanoparticles on exposed crystal surfaces and create subsurface nanoporosities.[25] Thus, an intriguing scenario emerges: AP7 protein phases focus their attention on PNC formation (Figure 4), and once calcium carbonate mineral nanopaticles form, the protein phases become active in the spatial assembly and organization of the mineral phase (Figures 5 and 6). These distinctive functions may ultimately determine the dimensional and material properties of nacre tablets,[1−7] and we are hopeful they will be explored in more detail.

The driving force behind these mineralization events is the ability of nacre proteins such as AP7 to form oligomeric assemblies (Figure 1A,B),[21,22] and this process is enhanced in the presence of Ca^{2+}-containing solutions (Figures 1C−E and 2). The AP7 oligomerization process was believed to be promoted by the aggregation-prone T31−N66 AA C-RING domain (Supporting Information, Figure S1),[22] and in the study presented here, we confirm this via NMR spectroscopy, where cross-peaks specific for this region were found to be attenuated (Figure 3); therefore, this region is most likely involved in intermolecular contacts within AP7 oligomers. In short, AP7 is an atypical C-RING protein that utilizes its modified RING sequence[21,22,25] for creating protein supramolecular assemblies that influence the mineralization process both in solution (Figures 4−6) and on crystal surfaces.[25] Note that the specific residues within T31−N66 that are involved in oligomeric intermolecular interactions have yet to be identified (Figure 3), and thus, additional experimentation will be required for their elucidation.

Our study provides new observations regarding the origins of molecular "disorganization" in AP7 protein complexes and an explanation for the amorphous, heterogeneous morphologies of AP7 oligomers that were originally noted in dynamic light scattering experiments.[22] We find that the -NG- rich D1−T19 N-terminal sequence region exists as a disordered, unrestrained, and labile region within assembled AP7 molecules (Figure 3), and this finding parallels the recent discovery of a disordered, labile -NG- rich T64−W98 segment within framework n16.3 protein phases.[28] Thus, while the T31−N66 C-RING sequence contributes to oligomer formation and stabilization, we believe that some degree of oligomer destabilization is concurrently introduced by the disordered D1−T19 N-terminal sequence. This leads to a molecular "conflict" within AP7 assemblies (Figure 1A,B), and this conflict manifests itself in the form of protein oligomers that possess polydispersity,[22] amorphous morphology, and movement (Figure 1A,B). Besides molecular destabilization, we believe that this disordered D1−T19 region could also play several important roles in AP7 function: (a) allowing AP7 oligomers to undergo the transition from small complexes into larger aggregates under appropriate conditions (Figures 1, 2, 5, and 6) and (b) facilitating protein phase compatibility with mineral nanoparticles (Figures 5 and 6)[55] that prolongs the time intervals for PNC formation (Table 1 and Figures 4−6). The finding that AP7 protein molecules within assemblies have persistent disordered regions has important consequences when one considers that more than 30 aragonite-associated proteins possess one or more intrinsically disordered sequence regions.[24] It may be that unfolded domains, such as the Asn, Gly repeats found within intracrystalline AP7 and the framework n16 protein family sequences,[27,28] are important for proteomic functions related to oligomerization, nucleation, and subsequent mineral organization in the nacre layer. We are hopeful that additional studies will determine the identity and role(s) of other intrinsically disordered sequences within the aragonite proteome.

Although we have documented the nonclassical nucleation and *in vitro* mineral organization capabilities of AP7 in this study, we were unable to address aragonite formation or stabilization by this protein, which we originally reported in earlier studies involving long-term ammonium carbonate vapor diffusion assays.[21] We believe that the absence of aragonite formation in the study presented here is most likely due to one or more of the following: (a) the choice of mineralization assay conditions, which may favor calcite over aragonite in short-duration experiments;[36,37] (b) the omission of aragonite-promoting agents, such as Mg^{2+}[55] or small metabolites,[56] which may be necessary for efficient aragonite formation; and (c) the fact that aragonite stabilization activity represents a minor *in vitro* function of the AP7 protein, as evidenced by the low efficiency (<10%) of aragonite formation generated by this protein in long-term diffusion assays.[21,22] This latter case is interesting in light of recent reports that mollusk shell-associated nacre proteins can actually block aragonite formation in favor of magnesium calcite formation.[53] We intend to follow up on these initial findings with additional experiments that probe *in vitro* aragonite formation in the presence of AP7 with additional agents.

Finally, the data presented here, when contrasted alongside results of recent studies[28] of the framework protein, n16.3 (*Pinctada fucata*),[10,12,13] reveal some interesting similarities and differences that exist between these nacre proteome representatives. Both AP7 and n16.3[28] oligomerize to form protein phases that assemble and organize mineral nanoparticles in solution. Thus, it is likely that framework and intracrystalline nacre proteins may have evolved a common ability to organize mineral nanoparticles, such that ordered aragonite tablets can eventually develop in the nacre layer. However, there are important proteomic distinctions with regard to the nucleation process: while AP7 protein phases prolong the time interval for

PNC formation and have no impact on postnucleation ACC stability or solubility, n16.3 protein phases have little effect on PNC formation but destabilize ACC clusters by increasing their solubilities.[28] Thus, although each representative protein organizes mineral nanoparticles, they evolved distinct preferences for influencing different stages of mineral nucleation (AP7, prenucleation; n16.3, postnucleation) that precede the mineral assembly process.[57] The ability to selectively control one or more aspects of the nonclassical nucleation scheme would afford intracrystalline and framework proteins the ability to tailor the nucleation or postnucleation processes for different regions (i.e., AP7, intracrystalline; n16.3, framework surface) of nacre tablets, such that the desired survival-dependent dimensional and material properties are achieved in the mature tissue. These concepts will be explored in subsequent studies.

■ ASSOCIATED CONTENT

Supporting Information

AP7 primary sequence and bioinformatics (Figure S1), AFM imaging of AP7 as a function of protein concentration (Figure S2), comparison of tapping mode AFM images of AP7 versus the nacre proteins PFMG1 and n16.3 (Figure S3), STEM video stills of protein-deficient calcium carbonate mineralization assays (Figure S4), STEM video stills of AP7 calcium carbonate mineralization assays (Figure S5), STEM video stills of AP7 agglomerations denoting angular facets and crystal formation (Figure S6), STEM flow cell video of calcium carbonate nucleation in the absence of AP7 (Movie S1), and STEM flow cell video of calcium carbonate nucleation in the presence of AP7 (Movie S2). This material is available free of charge via the Internet at http://pubs.acs.org.

■ AUTHOR INFORMATION

Corresponding Author

*Laboratory for Chemical Physics, Division of Basic Sciences, and Center for Skeletal Biology, New York University College of Dentistry, 345 E. 24th St., New York, NY 10010. E-mail: jse1@nyu.edu. Telephone: (212) 998-9605. Fax: (212) 995-4087.

Funding

H.C. and A.R. thank the Konstanz Research School of Chemical Biology for a Ph.D. stipend to A.R. We acknowledge support for A.V. and R.K. by the Engineering and Physical Sciences Research Council (Grant EP/I001514/1). Portions of this research (protein synthesis, AFM, NMR, and bioinformatics) were supported by the U.S. Department of Energy, Office of Basic Energy Sciences, Division of Materials Sciences and Engineering, via Contract DE-FG02-03ER46099.

Notes

The authors declare no competing financial interest.

■ ACKNOWLEDGMENTS

We acknowledge the JEOL Nanocentre for the electron microscope facilities. This report represents contribution 77 from the Laboratory for Chemical Physics, New York University.

■ ABBREVIATIONS

AP7, aragonite protein 7 from *Haliotis rufescens*; cAP7, chemically synthesized AP7 protein (66 amino acids); rAP7, *Escherichia coli* recombinant AP7 protein (67 amino acids); TEV, tobacco etch virus protease; $TrxHis_6$, recombinant thioredoxin poly$(His)_6$ affinity tag; STEM, scanning transmission electron microscopy; HAADF, high-angle annular dark field.

■ REFERENCES

(1) Southgate, P., and Lucas, J. (2008) in *The Pearl Oyster: A Beginner's Guide to Programming Images, Animation, and Interaction*, pp 77−102, Elsevier BV, Oxford, U.K.

(2) Xie, L.-P., Zhu, F.-J., Zhou, Y.-J., Uang, C., and Zhang, R.-Q. (2011) Molecular approaches to understand biomineralization of shell nacreous layer. In *Molecular Biomineralization, Progress in Molecular and Subcellular Biology* (Muller, W. E. G., Ed.) Vol. *52*, pp 331−352, Springer-Verlag, Berlin.

(3) Jäger, C., and Cölfen, H. (2007) Fine structure of nacre revealed by solid-state 13-C and 1-H NMR. *CrystEngComm 9*, 1237−1244.

(4) Nassif, N., Pinna, N., Gehrke, N., Antonetti, M., Jaer, C., and Colfen, H. (2005) Amorphous layer around aragonite platelets in nacre. *Proc. Natl. Acad. Sci. U.S.A. 102*, 12653−12655.

(5) Yan, Z., Ma, Z., Zheng, G., Feng, Q., Wang, H., Xie, L., and Zhang, R. (2008) The inner-shell film: An intermediate structure participating in pearl oyster shell formation. *ChemBioChem 9*, 1093−1099.

(6) Checa, A. G., Cartwright, J. H. E., and Willinger, M. G. (2009) The key role of the surface membrane in why gastropod nacre grows in towers. *Proc. Natl. Acad. Sci. U.S.A. 106*, 38−43.

(7) Falini, G., Albeck, S., Weiner, S., and Addadi, L. (1996) Control of aragonite or calcite polymorphism by mollusk shell macromolecules. *Science 271*, 67−69.

(8) Kinoshita, S., Wang, N., Inoue, H., Maeyama, K., Okamoto, K., Nagai, K., Kondo, H., Hirono, I., Asakawa, S., and Watabe, S. (2011) Deep sequencing of ESTs from nacreous and prismatic layer producing tissues and a screen for novel shell formation-related genes in the pearl oyster. *PLoS One 6*, 1−19.

(9) Marie, B., Joubert, C., Tayale, A., Zanella-Cleon, I., Belliard, C., Piquemal, D., Cochennec-Laureau, N., Marin, F., Gueguen, Y., and Montagnani, C. (2012) Different secretory repertoires control the biomineralization processes of prism and nacre deposition of the pearl oyster shell. *Proc. Natl. Acad. Sci. U.S.A. 109*, 20986−20991.

(10) Nogawa, C., Baba, H., Masaoka, T., Aoki, H., and Samata, T. (2012) Genetic structure and polymorphisms of the N16 gene in *Pinctada fucata*. *Gene 504*, 84−91.

(11) Gardner, L. D., Mills, D., Wiegand, A., Leavesley, D., and Elizur, A. (2011) Spatial analysis of biomineralization associated gene expression from the mantle organ of the pearl oyster, *Pinctada maxima*. *BMC Genomics 12*, 455−470.

(12) Fang, D., Xu, G., Hu, Y., Pan, C., Xie, L., and Zhang, R. (2011) Identification of genes directly involved in shell formation and their functions in pearl oyster, *Pinctada fucata*. *PLoS One 6*, 1−13.

(13) Zhang, G., et al. (2012) The oyster genome reveals stress adaptation and complexity of shell formation. *Nature 490*, 49−54.

(14) Nudleman, F., Shimoni, E., Klein, E., Rousseau, M., Bourrat, X., Lopez, E., Addadi, L., and Weiner, S. (2008) Forming nacreous layer of the shells of the bivalves *Atrina rigida* and *Pinctada margaritifera*: An environmental- and cryo-scanning electron microscopy study. *J. Struct. Biol. 162*, 290−300.

(15) Michenfelder, M., Fu, G., Lawrence, C., Weaver, J. C., Wustman, B. A., Taranto, L., and Evans, J. S. (2003) Characterization of two molluscan crystal-modulating biomineralization proteins and identification of putative mineral binding domains. *Biopolymers 70*, 522−533.

(16) Fu, G., Qiu, R., Orme, C. A., Morse, D. E., and De Yoreo, J. J. (2005) Acceleration of calcite kinetics by abalone nacre proteins. *Adv. Mater. 17*, 2678−2683.

(17) Weiss, I. M., Kaufmann, S., Mann, K., and Fritz, M. (2000) Purification and characterization of perlucin and perlustrin, two new proteins from the shell of the mollusc *Haliotis laevigata*. *Biochem. Biophys. Res. Commun. 267*, 17−21.

(18) Yan, Z., Fang, Z., Ma, Z., Deng, J., Li, S., Xie, L., and Zhang, R. (2007) Biomineralization: Functions of calmodulin-like protein in the shell formation of pearl oyster. *Biochim. Biophys. Acta 1770*, 1338–1344.
(19) Ramos-Silva, P., Benhamada, S., Le Roy, N., Marie, B., Guichard, N., Zanella-Clon, I., Plasseraud, L., Corneillat, M., Alcaraz, G., Kaandorp, J., and Marin, F. (2012) Novel molluskan biomineralization proteins retrieved from proteomics. A case study with upsalin. *ChemBioChem 13*, 1067–1078.
(20) Marie, B., Joubert, C., Tayale, A., Zanella-Cleon, I., Belliard, C., Piquemal, D., Cochennec-Laureau, N., Marin, F., Gueguen, Y., and Montagnani, C. (2012) Different secretory repertoires control the biomineralization processes of prism and nacre deposition of the pearl oyster shell. *Proc. Natl. Acad. Sci. U.S.A. 109*, 20986–20991.
(21) Amos, F. F., and Evans, J. S. (2009) AP7, a partially disordered pseudo C-RING protein, is capable of forming stabilized aragonite in vitro. *Biochemistry 48*, 1332–1339.
(22) Amos, F. F., Ndao, M., Ponce, C. B., and Evans, J. S. (2011) A C-RING-like domain participates in protein self-assembly and mineral nucleation. *Biochemistry 50*, 8880–8887.
(23) Collino, S., Kim, I. W., and Evans, J. S. (2008) Identification and structural characterization of an unusual RING-like sequence within an extracellular biomineralization protein, AP7. *Biochemistry 47*, 3745–3755.
(24) Evans, J. S. (2012) Identification of intrinsically disordered and aggregation: Promoting sequences within the aragonite-associated nacre proteome. *Bioinformatics 28*, 3182–3185.
(25) Chang, E. P., Russ, J. A., Verch, A., Kroeger, R., Estroff, L. A., and Evans, J. S. (2014) Engineering of crystal surfaces and subsurfaces by an intracrystalline biomineralization protein. *Biochemistry 53*, 4317–4319.
(26) Perovic, I., Mandal, T., and Evans, J. S. (2013) A pearl protein self-assembles to form protein complexes that amplify mineralization. *Biochemistry 52*, 5696–5703.
(27) Ponce, C. B., and Evans, J. S. (2011) Polymorph crystal selection by n16, an intrinsically disordered nacre framework protein. *Cryst. Growth Des. 11*, 4690–4696.
(28) Perovic, I., Chang, E. P., Lui, M., Rao, A., Cölfen, H., and Evans, J. S. (2014) A framework nacre protein, n16.3, self-assembles to form protein oligomers that participate in the post-nucleation spatial organization of mineral deposits. *Biochemistry 53*, 2739–2748.
(29) Chang, E. P., Russ, J. A., Verch, A., Kroeger, R., Estroff, L. A., and Evans, J. S. (2014) Engineering of crystal surfaces and subsurfaces by framework biomineralization protein phases. *CrystEngComm 16*, 7406–7409.
(30) Gebauer, D., Volkel, A., and Cölfen, H. (2008) Stable prenucleation of calcium carbonate clusters. *Science 322*, 1819–1822.
(31) Gebauer, D., and Cölfen, H. (2011) Prenucleation clusters and non-classical nucleation. *Nano Today 6*, 564–584.
(32) Demichelis, R., Raiteri, P., Gale, J. D., Quigley, D., and Gebauer, D. (2011) Stable prenucleation mineral clusters are liquid-like ionic polymers. *Nat. Commun. 2*, 1–8.
(33) Gebauer, D., Cölfen, H., Verch, A., and Antonietti, M. (2008) The multiple roles of additives in $CaCO_3$ crystallization: A quantitative case study. *Adv. Mater. 21*, 435–439.
(34) Verch, A., Gebauer, D., Antonietti, M., and Cölfen, H. (2011) How to control the scaling of $CaCO_3$: A "fingerprinting technique" to classify additives. *Phys. Chem. Chem. Phys. 13*, 16811–16820.
(35) Rao, A., Berg, J. K., Kellermeier, M., and Gebauer, D. (2014) Sweet on biomineralization: Effect of carbohydrates on the early stages of calcium carbonate crystallization. *Eur. J. Mineral.*, DOI: 10.1127/0935-1221/2014/0026-2379.
(36) Stephens, C. J., Kim, Y. Y., Evans, S. D., Meldrum, F. C., and Christenson, H. K. (2011) Early stages of crystallization of calcium carbonate revealed in picoliter droplets. *J. Am. Chem. Soc. 133*, 5210–5213.
(37) Stephens, C. J., Ladden, S. F., Meldrum, F. C., and Christenson, H. K. (2010) Amorphous calcium carbonate is stabilized in confinement. *Adv. Mater. 2010 20*, 2108–2115.
(38) Wishart, D. S., and Nip, A. M. (1998) Protein chemical shift analysis. A practical guide. *Biochem. Cell Biol. 76*, 153–163.
(39) Kjaergaard, M., and Poulsen, F. M. (2011) Sequence correction of random coil chemical shifts: Correlation between neighbor correction factors and changes in the Ramachandran distribution. *J. Biomol. NMR 50*, 157–165.
(40) Sibley, A. B., Cosman, M., and Krishnan, V. V. (2005) An empirical correlation between secondary structure content and averaged chemical shifts in proteins. *Biophys. J. 84*, 1223–1227.
(41) Kim, D. T., Blanch, H. W., and Radke, C. J. (2002) Direct imaging of aqueous lyzozyme adsorption onto mica by atomic force microscopy. *Langmuir 18*, 5841–5850.
(42) He, G., Dahl, T., Veis, A., and George, A. (2003) Nucleation of apatite crystals in vitro by self-assembled dentin matrix protein 1. *Nat. Mater. 2*, 552–558.
(43) Bromley, K. M., Kiss, A. S., Lokappa, S. B., Lakshminarayanan, R., Fan, D., Ndao, M., Evans, J. S., and Moradian-Oldak, J. (2011) Dissecting amelogenin nanospheres: Characterization of metastable oligomers. *J. Biol. Chem. 286*, 34643–34653.
(44) Delak, K., Harcup, C., Lakshminarayanan, R., Zhi, S., Fan, Y., Moradian-Oldak, J., and Evans, J. S. (2009) The tooth enamel protein, porcine amelogenin, is an intrinsically disordered protein with an extended molecular configuration in the monomeric form. *Biochemistry 48*, 2272–2281.
(45) Ndao, M., Dutta, K., Bromley, K., Sun, Z., Lakshminarayanan, R., Rewari, G., Moradian-Oldak, J., and Evans, J. S. (2011) Probing the self-association, intermolecular contacts, and folding propensity of amelogenin. *Protein Sci. 20*, 724–734.
(46) Ndao, M., Ponce, C. B., and Evans, J. S. (2012) Oligomer formation, metalation, and the existence of aggregation-prone and mobile sequences within the intracrystalline protein family, Asprich. *Faraday Discuss. 159*, 449–462.
(47) Biological Magnetic Resonance Databank (http://www.bmrb.wisc.edu/ref_info/statful.htm).
(48) Uversky, V. N. (2002) Natively unfolded proteins: A point where biology waits for physics. *Protein Sci. 11*, 739–756.
(49) Tompa, P. (2002) Intrinsically unstructured proteins. *Trends Biochem. Sci. 27*, 527–533.
(50) Meng, J., Romero, P., Yang, J. Y., Chen, J. W., Vacic, V., Obradovic, Z., and Uversky, V. N. (2008) The unfoldomics decade: An update on intrinsically disordered proteins. *BMC Genomics 9*, 1–26.
(51) Peysselon, F., Xue, B., Uversky, V. N., and Ricard-Blum, S. (2011) Intrinsic disorder of the extracellular matrix. *Mol. BioSyst. 7*, 3353–3365.
(52) Kim, I. W., Morse, D. E., and Evans, J. S. (2004) Molecular characterization of the 30-AA N-terminal mineral interaction domain of the biomineralization protein AP7. *Langmuir 20*, 11664–11673.
(53) Picker, A., Kellermeier, M., Seto, J., Gebauer, D., and Cölfen, H. (2012) The multiple effects of amino acids on the early stages of calcium carbonate crystallization. *Z. Kristallogr. 227*, 744–757.
(54) Gebauer, D., Gunawidjaja, P. N., Ko, J. Y. P., Bacsik, Z., Aziz, B., Liu, L., Hu, Y., Bergström, L., Tai, C.-W., Sham, T.-K., Edén, M., and Hedin, N. (2010) Proto-calcite and proto-vaterite in amorphous calcium carbonates. *Angew. Chem., Int. Ed. 49*, 8889–8891.
(55) Pan, C., Fang, D., Xu, G., Liang, J., Zhang, G., Qwang, H., Xie, L., and Zhang, R. (2013) A novel acidic matrix protein, PfN44, stabilizes magnesium calcite to inhibit the crystallization of aragonite. *J. Biol. Chem. 289*, 2776–2787.
(56) Sato, A., Nagasaka, S., Furihata, K., Nagata, S., Arai, I., Saruwatari, K., Kogure, T., Sakuda, S., and Nagasawa, H. (2011) Glycolytic intermediates induce amorphous calcium carbonate formation in crustaceans. *Nat. Chem. Biol. 7*, 197–199.
(57) Evans, J. S. (2013) "Liquid-like" biomineralization protein assemblies: A key to the regulation of non-classical nucleation. *CrystEngComm 15*, 8388–8394.